




Canopy Averaged Chlorophyll Content Prediction of Pear Trees Using Convolutional Autoencoder on Hyperspectral Data

Subir Paul , Vinayaraj Poliyapram , Nevrez İmamoğlu , Kuniaki Uto , Ryosuke Nakamura, and D. Nagesh Kumar 

Abstract—Chlorophyll content is one of the essential parameters to assess the growth process of the fruit trees. This present study developed a model for estimation of canopy averaged chlorophyll content (CACC) of pear trees using the convolutional autoencoder (CAE) features of hyperspectral (HS) data. This study also demonstrated the inspection of anomaly among the trees by employing multidimensional scaling on the CAE features and detected outlier trees prior to fit nonlinear regression models. These outlier trees were excluded from the further experiments that helped in improving the prediction performance of CACC. Gaussian process regression (GPR) and support vector regression (SVR) techniques were investigated as nonlinear regression models and used for prediction of CACC. The CAE features were proven to be providing better prediction of CACC when compared with the direct use of HS bands or vegetation indices as predictors. The CACC prediction performance was improved with the exclusion of the outlier trees during training of the regression models. It was evident from the experiments that GPR could predict the CACC with better accuracy compared to SVR. In addition, the reliability of the tree canopy masks, which were utilized for averaging the features' values for a particular tree, was also evaluated.

Index Terms—Canopy averaged chlorophyll content (CACC), convolutional autoencoder (CAE), deep learning, Gaussian process regression (GPR), hyperspectral (HS) data, pear orchard.

I. INTRODUCTION

GLOBAL food demand is rising rapidly with an increase in population. In order to meet the increasing demand, food

Manuscript received December 6, 2019; revised February 1, 2020, February 28, 2020, and March 9, 2020; accepted March 17, 2020. Date of publication March 30, 2020; date of current version April 21, 2020. This work was conducted at the National Institute of Advanced Industrial Science and Technology (AIST) and supported in part by AIST, the New Energy and Industrial Technology Development Organization (NEDO), and in part by AIST-Tokyo Tech Real World Big-Data Computation—Open Innovation Laboratory (RWBC-OIL), Tokyo, Japan. (Corresponding author: Subir Paul.)

Subir Paul and D. Nagesh Kumar are with the Department of Civil Engineering, Indian Institute of Science, Bengaluru 560012, India (e-mail: subir.paul.iisc@gmail.com; nagesh@iisc.ac.in).

Vinayaraj Poliyapram is with the National Institute of Advanced Industrial Science and Technology (AIST)-Tokyo Tech Real World Big-Data Computation Open Innovation Laboratory (RWBC-OIL), Tokyo 152-8550, Japan (e-mail: vinay223333@gmail.com).

Nevrez İmamoğlu and Ryosuke Nakamura are with the Artificial Intelligence Research Center, National Institute of Advanced Industrial Science and Technology (AIST), Tokyo 135-0064, Japan (e-mail: nevrez.imamoglu@aist.go.jp; r.nakamura@aist.go.jp).

Kuniaki Uto is with the School of Computing, Tokyo Institute of Technology, Tokyo 152-8550, Japan (e-mail: uto@c.titech.ac.jp).

Digital Object Identifier 10.1109/JSTARS.2020.2983000

production should be improved. Continuous health monitoring of plants or crops during their growing period can help in maximizing food production or yield by identifying diseases, stress conditions or any other issues and taking necessary steps to resolve those issues [1]–[3]. Chlorophyll content is a vital biochemical parameter and a major indicator of the growth process, photosynthetic activity, developmental stage, nutritional, and physiological status of fruit trees [4], [5], vegetables (or crops) [6], and other types of plants [7]. Disease detection, maturity of crops or vegetation and prediction of primary production or yield can be assessed with the estimation of chlorophyll content [8], [9]. Chlorophyll content can be estimated using chlorophyll content meter, optical contact sensor such as soil plant analysis development (SPAD) 502 of Minolta, images of airborne cameras, and multispectral and hyperspectral (HS) images [1]. Chlorophyll content meter and SPAD are most useful for rapid and nondestructive *in situ* estimation of leaf chlorophyll content (LCC) but not suitable for estimation of canopy averaged chlorophyll content (CACC) or canopy chlorophyll content (CCC) of tall plants [9]. In-field chlorophyll content estimation techniques are labor intensive, time consuming, expensive and do not provide real-time monitoring. Remote sensing data can be considered as a reliable solution for continuous spatial and temporal monitoring of chlorophyll content.

Numerous studies have used remote sensing data for chlorophyll content monitoring of different types of plants. Pérez-Patricio *et al.* [1] estimated chlorophyll content of plant leaves using the reflectance and transmittance of Red–Green–Blue (RGB) images. Ma *et al.* [9] constructed a three-layer artificial neural network (ANN) [10] model for prediction of chlorophyll content in different light areas of apple tree canopies. Degerickx *et al.* [11] estimated chlorophyll content and leaf area index (LAI) to assess the health of urban trees using HS and LIDAR data. CCC estimation of fruit trees was attempted in different studies using the spaceborne sensor data [4], [8]. Li *et al.* [8] estimated CCC of apple trees using Sentinel-2A data. However, coarse spatial and spectral resolution of these data and cloudy-sky condition effect the precise and continuous estimation of CCC or CACC [12]. The critical issues of spaceborne (e.g., spatial and spectral resolution, real-time monitoring, cloudy-sky) and airborne (e.g., high operational cost) sensors can be overcome with the use of low cost unmanned aerial vehicle (UAV)

system [13]. Hence, Vanbrabant *et al.* [12] used remotely piloted aircraft systems (RPAS) for the acquisition of remote sensing images, which are flexible enough in revisit time with very fine spatial resolution, and have less dependency on weather conditions.

Biophysical (e.g. LAI, biomass) and biochemical (e.g. chlorophyll and nitrogen content) variables retrieval methods using optical remote sensing images can be categorized into 1) parametric regression, 2) nonparametric regression, 3) physically-based (i.e., radiative transfer models), and 4) hybrid methods (e.g., a combination of physically-based and nonparametric nonlinear regression methods) [14]. Several parametric and nonparametric approaches were evaluated for modeling of different biophysical and biochemical variables. Parametric regression techniques use limited or optimally selected spectral bands or vegetation indices [1] for modeling. Numerous spectral band indices or VIs, viz., normalized difference vegetation index [15], photochemical reflectance index [16], [17], optimized soil-adjusted vegetation index (OSAVI) [18], modified chlorophyll absorption in reflectance index (MCARI) [19], transformed chlorophyll absorption in reflectance index [20], greenness vegetation index [21], and triangular greenness index (TGI) [22], were developed for detection or estimation of LCC or CACC or CCC. VIs can be used in nonparametric models [e.g., ANN, support vector regression (SVR)] too for estimation of CACC or CCC [8]. However, these indices do not exploit the ample spectral information of HS data and instead these consider only 2–5 specific spectral bands [12], [23], which may be apt for local applications but lack general applicability [14]. Though VIs can be calculated using spectral reflectances of narrow-bands, VIs-based methods are more suited to broadband spectral data [14]. Nonparametric models do not make any assumptions about the data distribution and dependencies between variables as in the case of parametric models. Gaussian process regression (GPR) technique was introduced in Verrelst *et al.* [23] for overcoming the limitations of other nonparametric models, viz., ANN [9], SVR [24], [25], and relevance vector machine [26], for retrieval of biophysical and biochemical variables. Radiative transfer modeling is a more challenging task compared to parametric and nonparametric regression because of several issues, such as more unknowns compared to observation points, computational resources, and requirement of experimental data for calibration [14].

Deep learning networks have been proven to be very effective in discovering low-level (e.g., edges) and mid-level (e.g., shapes) structures from a dataset [27]. Though deep learning techniques can be computationally expensive, several applications in classification studies using high-dimensional datasets (e.g., HS data) have proven the effectiveness of the deep learning algorithms. Deep learning techniques, such as autoencoder (AE) or stacked autoencoder (SAE) demonstrate salient feature representation of high-dimensional datasets (e.g., HS data), which were efficiently used in classification applications [28]–[31]. Convolutional autoencoder (CAE), a combination of convolution operation of convolutional neural network and self-supervised learning of AE, was utilized for 3-D object retrieval [32], deep unsupervised feature representation and subsequently for classification of high-resolution remote sensing images [33], and SAR images [27]. CAE reduces the computational parameters for feature

extraction as compared to AE [33], and can be considered as an improved spectral-spatial deep feature extraction technique over spectral deep feature extraction technique SAE. The CAE extracted features can be used in classification or regression tasks in two ways, either by including a neural network layer at the end and training the whole architecture altogether or by using trained CAE features in a different classifier or regression learner.

Remote sensing data-based LCC or CACC or CCC prediction techniques mostly consider VIs in the regression model, which do not exploit the full potential of HS data. Though, a few studies attempted to use the whole spectrum of HS data but these studies did not address the issue of redundant information present in the HS data. Redundancy of HS data can be removed by employing dimensionality reduction techniques. In this article, we have proposed the use of unsupervised spectral-spatial features of HS data, extracted by CAE, for fitting in regression models and predicting CACC of Pear trees. The CAE features were utilized for detection of outlier trees to be eliminated in order to improve the performance of CACC prediction. Multidimensional scaling (MDS) technique was utilized for outlier detection [34]. After removal of outlier trees, CAE features of rest of the trees were utilized in GPR or SVR for model fitting and CACC prediction. A brief overview of the work is presented in Fig. 1.

The major objectives of this article are as follows.

- 1) Taking advantage of unsupervised representation learning for high level features extraction by implementing a relatively small CAE network on the HS data.
- 2) Extensive investigations of the unsupervised CAE features of HS data to predict CACC and demonstration of improvements compared to the baseline approach [12].
- 3) Analysis of the deep high-level CAE representations by taking advantage of MDS to embed high-dimensional tree canopy features in low-dimensional two-dimensional (2-D) space, and to compare each tree with respect to others to find out anomaly among trees (i.e., outlier trees) in the orchard.

The rest of this article is organized as follows. Section II provides the details about the study area and datasets. In Section III, the methodology of outlier tree detection using MDS and fitting regression models and CACC prediction using CAE features are presented. In Section IV, results from different experiments are reported. Section V presents the discussion of the experimental results. Finally, Section VI concludes this article.

II. STUDY AREA AND DATASETS

This work was carried out for a Pear orchard (14 years old “Conference” trees) [12], located in Belgium (see Fig. 2). The dataset was acquired by HYPERTEMP project group and made available as a part of BELAIR HESBANIA 2017 project [12]. The tree canopy areas of 178 Pear trees were provided in this dataset. HS image acquisitions were done covering these trees in the orchard for the growing period (May–October, 2017). However, this dataset includes reference CACC of only 33 trees for the growing period (May–October, 2017).

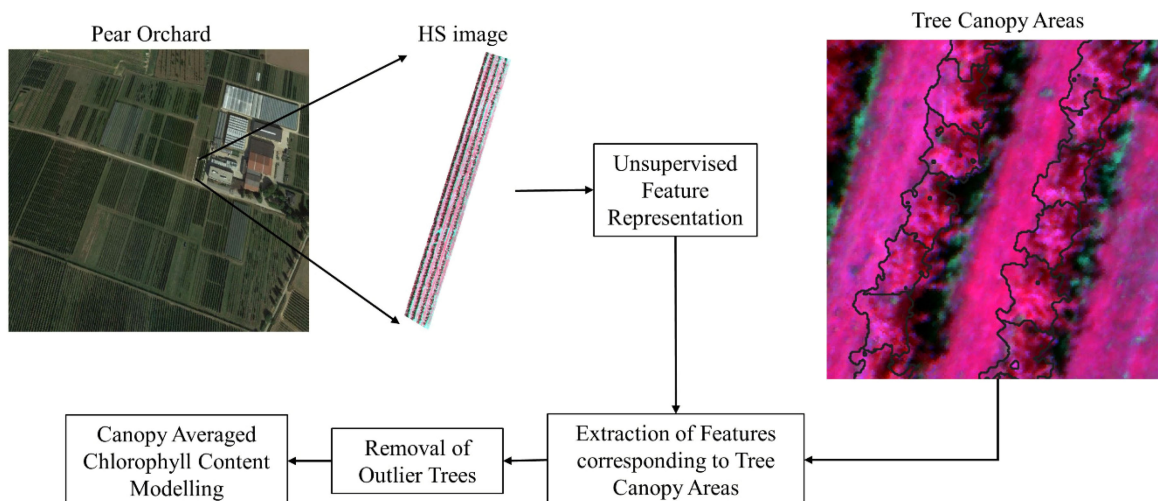


Fig. 1. Brief overview of the present work (Images source: Google Earth and BELAIR HESBANIA 2017 dataset).

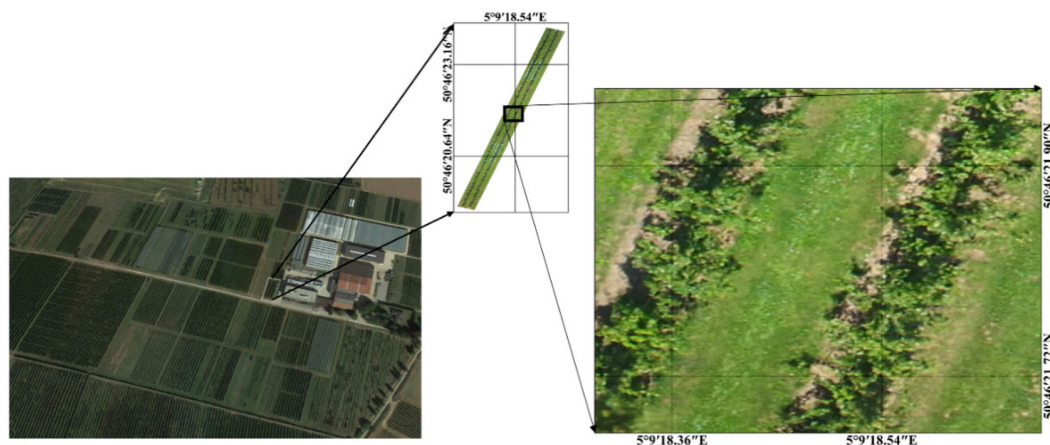


Fig. 2. Location of the pear orchard (Images source: Google Earth and BELAIR HESBANIA 2017 dataset).

A. HS Data

The HS images were acquired using the Headwall Micro-Hyperspec¹ during the pear fruit growing period (May–October) of 2017 [12]. The HS sensor was mounted on a UAV platform which is Altura Zenith ATX8 rotorcraft (Aerialtronics, the Netherlands). The HS images comprised spectral information of 326 bands (with ~ 2 nm bandwidth and covering the spectral range of 400–1000 nm) at 5 cm spatial resolution. Geometric and radiometric calibrations of the HS images were performed using ground control points and spectral reference targets. Geometric correction was performed based on direct geo-referencing using VITO-developed C++ module. Further details about radiometric and spectral calibration and geometric correction processes can be found in Vanbrabant *et al.* [12]. Vanbrabant *et al.* [12] found that the spectral bands of around 400 nm and 900–1000 nm

were noisy. Hence, only the spectral bands in the range of 405–895 nm were considered as noise free in this study, which result in 264 spectral bands. However, they have used 280 spectral bands for their analysis, which considered few spectral bands from the noisy region. We have investigated two experiments, first considering all possible combinations of continuous 280 spectral bands, since the exact spectral region was not specified in Vanbrabant *et al.* [12]; and second after removing the noisy bands only 264 bands (405–895 nm) were utilized for CACC prediction. It was observed that 264 spectral bands combination, which did not include any noisy bands, performed better. Hence, in order to remove the effect of noisy data, we have utilized only the 264 spectral bands (405–895 nm) for further analysis in this study. Table I [12] presents the acquisition dates and times of HS images for different growth-stages of pear trees. However, the dataset contains reference CACC only for three months (i.e., June, July, and October), and the HS image of October month does not cover all the reference trees. Hence, we have utilized 33 reference pear trees for June and July months but in case of

¹<https://www.headwallphotonics.com/hyperspectral-sensors>

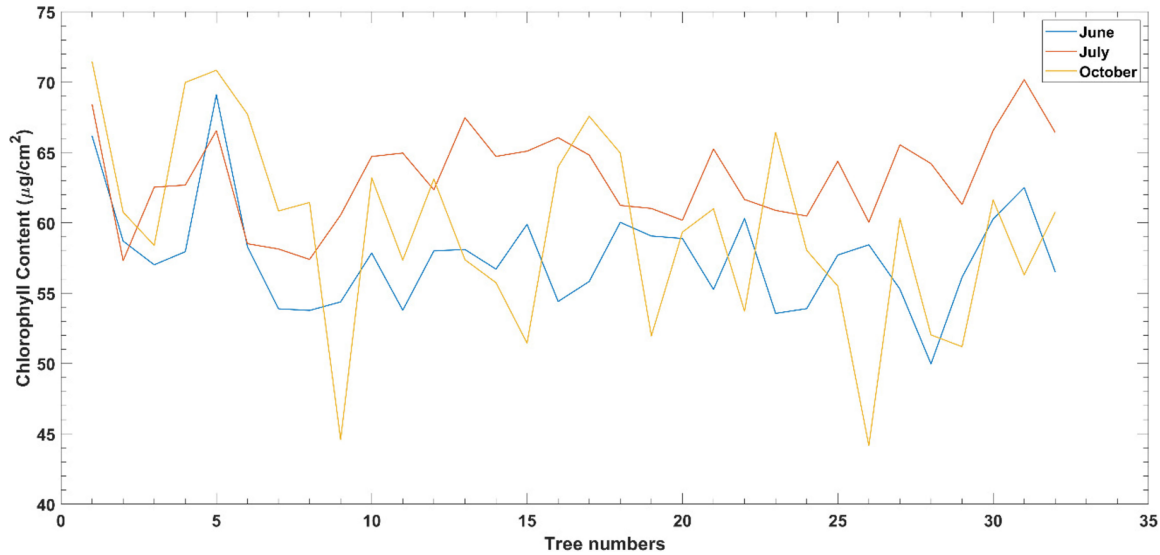


Fig. 3. Month-wise CACC ($\mu\text{g}/\text{cm}^2$) of experimental trees.

TABLE I
DETAILS OF THE HS RPAS FLIGHT DATES AND CORRESPONDING
GROWTH-STAGES OF THE PEAR TREES

Date	Time	Growth-stage
17-05-2017	03:58 – 04:06 pm	Fruit fall after flowering
14-06-2017	01:17 – 01:26 pm	Second fruit fall
13-07-2017	02:20 – 02:27 pm	Fruit growth and ripening
22-08-2017	11:24 – 11:32 am	Fruit ripe for picking
16-10-2017	03:29 – 03:35 pm	Leaf senescence

October month, only 17 trees were utilized for CACC modeling (i.e., data for tree IDs (TIDs) 2–15, 23, and 24 were not included in the published dataset). The details about the 33 experimental trees (i.e., TIDs among 178 trees) are available in the BELAIR HESBANIA 2017 dataset [12].

B. Canopy Averaged Chlorophyll Content

The reference CACC was retrieved for 33 experimental pear trees during the different growing stages. Reference CACC of each tree was calculated by averaging the LCC estimates of 20 sampled leaves, collected randomly from all parts of the canopy, of that tree [12]. However, BELAIR HESBANIA 2017 dataset comprises/consists of CACC estimates of only three months' (i.e., June, July, and October) of growth stages. The reference CACC of all trees for the observed three months of growing period are shown in Fig. 3. The ranges of the reference CACC are 49.97–69.11, 57.31–70.17, and 44.16–71.47 $\mu\text{g}/\text{cm}^2$, respectively, for June, July, and October months. The reference trees had higher CACC values in July compared to June month, since the tree canopies were in optimal growth condition with complete growth and ripening of fruits during the July month. October month was the leaf senescence period, when aging of leaves started and the color of leaves changed. However, aging conditions of leaves of different trees might vary, which resulted to inconsistency in the CACC observations of the trees during October.

III. METHODOLOGY

The workflow of the CACC prediction is presented in Fig. 4. In the first step, all the potential noisy bands are removed and rest of the bands (264 bands starting from 405 to 895 nm with intervals of ~ 2 nm) are utilized for further analysis. Then, CAE is employed on the 264 bands for extraction of spectral-spatial features from the data. This part of the workflow (i.e., CAE network) is highlighted with a dotted line box and the detailed architecture is presented in Fig. 5. The pixels falling within the canopy area of each tree are identified and their feature values are averaged to calculate an average feature representation corresponding to each tree. Averaging the feature values in the canopy area of a tree is well-suited practice for our experiments since the reference CACCs are average representation of chlorophyll content of the whole canopy of a tree. In the next step, these average CAE features are used to identify outlier trees. Outlier trees are identified with the help of MDS and visualizing the trees in a 2-D scatter plot. After removal of the outlier trees, average CAE features of the rest of the tree samples are utilized for training (or fitting) the nonparametric models viz., GPR and SVR and prediction of CACC.

A. Convolutional Autoencoder (CAE) for Unsupervised Representation Learning

CAE is a deep learning based unsupervised feature representation algorithm. CAE is designed based on the same principle of encoder and decoder of AE but it replaces the fully connected layers of AE with convolution layers, which reduce the number of parameters and provides a better representation of the data [35], [36]. CAE extracts the spectral-spatial features from the data.

Being a deep learning or high-level feature extraction method, CAE can be computationally expensive compared to traditional feature extraction strategies such as principal component analysis, but it has significant importance in deriving features

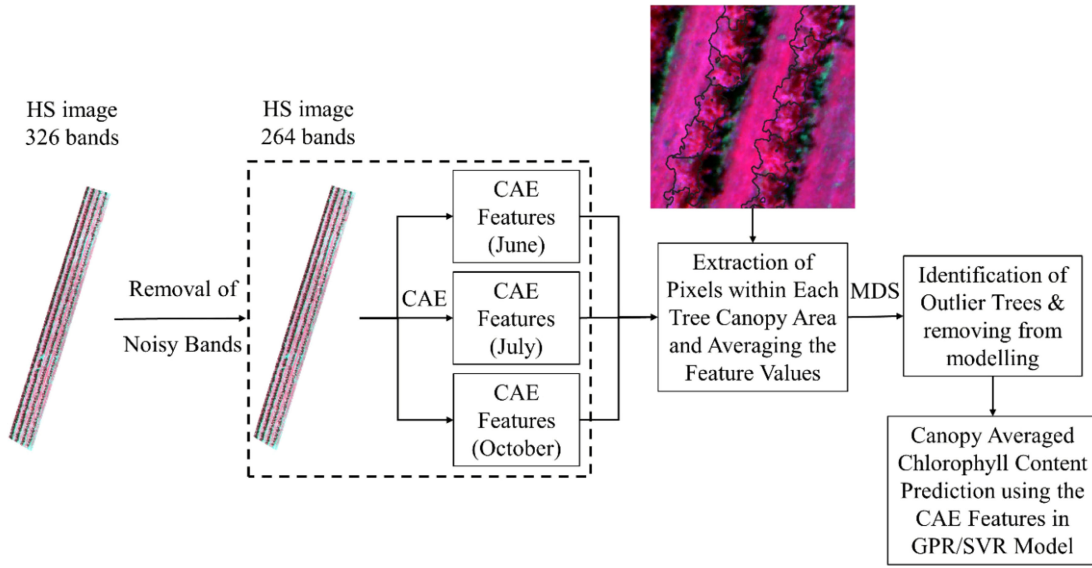


Fig. 4. Workflow of CACC prediction.

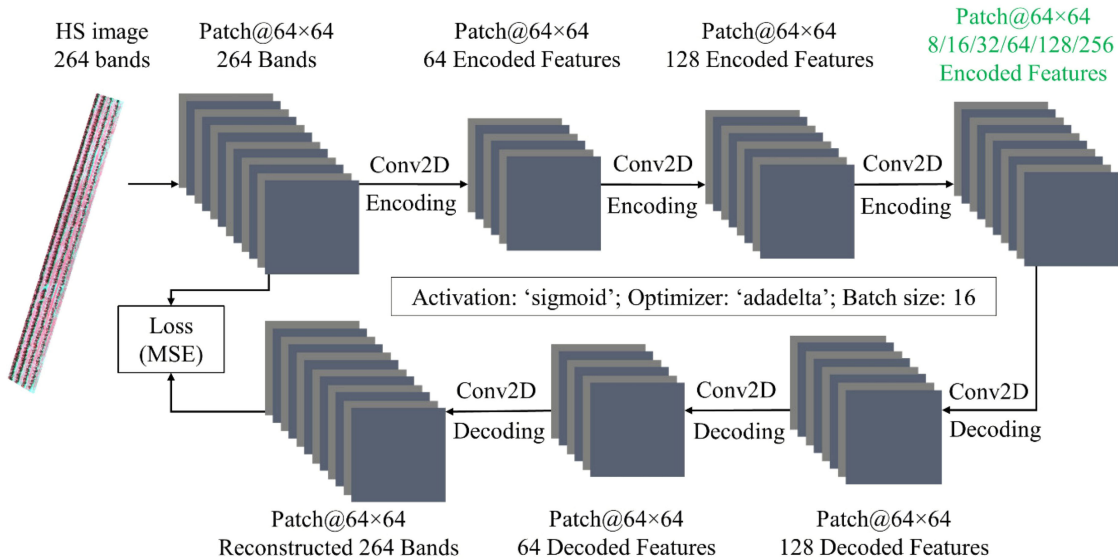


Fig. 5. Proposed CAE architecture.

which may not be produced by traditional feature extraction approaches.

Compared to other well-known deep learning-based unsupervised feature representation such as AE and SAE, the CAE requires less number of computational parameters to be trained [32], and hence it is computationally efficient compared to AE and SAE.

CAE introduces 2-D, 3×3 kernel-based weights and convolve through HS data and hence it is efficient to preserve neighborhood relationship and local features.

In this work, CAE network is employed with three encoding and three decoding layers. The architecture of CAE is presented in Fig. 5. The filter size of last encoding layer is varied from 8 to 256 (i.e., 8, 16, 32, 64, 128, and 256) to investigate

the performances of different numbers of features in CACC modeling. The CAE network is trained considering “sigmoid” activation function for all encoding and decoding layers with “AdaDelta” [37] optimizer. Mean squared error (MSE) has been used for loss calculation between original and reconstructed data. The HS image is divided into patches of size 64×64 and CAE network is trained with batch size of 16.

B. Use of High-level Encoded Features for Similarity Comparison to Detect Outlier Trees

MDS [38] is a visual representation of distances or dissimilarities between sets of objects. The averaged CAE features of each tree canopy area are used to calculate pairwise dissimilarities

between all combinations of two trees using Euclidian distance. MDS uses the dissimilarity matrix to create 2-D variables. These 2-D variables are plotted in a 2-D plot to visualize the reference tree samples. Trees that are more similar (or have shorter distances) are closer together on the graph than the trees that are less similar (or have longer distances). Hence, outlier trees can be identified from this 2-D plot, being located away of the common cluster of rest of the trees.

C. CACC Prediction

GPR has been proven to be an effective tool for retrieval of vegetation biophysical and biochemical variables using multi-spectral or HS data [23]. Vanbrabant *et al.* [12] utilized numerous linear and nonlinear models for prediction of CACC using the HS data. It was found that nonparametric and nonlinear regression models viz., GPR and SVR with Gaussian radial basis function (RBF) kernel provide more or less consistent performance. Therefore, we have adopted GPR and SVR along with Gaussian RBF kernel to fit the models using the CAE features of HS data and for prediction of CACC.

GPR is a stochastic process or probabilistic model. GPR learns the relationship between input (i.e., HS bands or CAE features) and output (i.e., CACC) variables by fitting nonlinear and nonparametric model to the data. GPR models the response or output variable by introducing latent variables (i.e., function of input variables) from a Gaussian process.

SVR uses the principle of support vector machine (SVM) algorithm for classification with some minor changes, since in case of SVR output is a real number. The basic concept of SVR is same as SVM viz., minimization of error, and individualize the hyperplane by maximizing the margin. The nonlinear kernel functions transform the data into a high dimensional feature space for linear separation of the data in the new transformed space.

D. Experimental Setup

The experiments were carried out on a Desktop PC (CPU: Intel Core i5-6500 @ 3.20 GHz, GPU: Nvidia GeForce GTX 1070 8GB, RAM: 32 GB DDR4) using Python and R programming languages. Extraction of CAE features was performed using the Python-based deep learning library “Keras” [39]. The R package “kernelab” has been used for fitting the GPR and SVR models using the high-level CAE features as input variables to predict the CACC of each tree. The whole HS images were divided into patches of size (64 × 64) and these patches are partitioned into three parts viz., training, validation, and testing datasets for CAE feature extraction process. All the patches were combinations of pixels from tree canopy area and background area. The patches having the reference tree canopy areas were considered as testing data, and the rest of the patches are randomly divided into training and validation data considering 80% and 20% patches, respectively. The CAE network was trained five times for generalization of the extracted CAE features. In case of CACC prediction, the reference tree samples were divided into two parts viz., training and testing data considering 70% and 30% of the samples, respectively. Ten trials were performed for CACC

modeling of each experiment considering random partitioning of training and testing data in each trial. At the end, average and standard deviation (SD) of the performance evaluation metrics from all trials are reported for each experiment, which will be demonstrated in the following sections.

E. Performance Evaluation Metrics

The performances of CACC modeling were evaluated with four different performance evaluation metrics viz., Pearson correlation coefficient (r), Nash–Sutcliffe efficiency index (NSE), root mean square error (RMSE), and normalized RMSE (NRMSE) as were used in Vanbrabant *et al.* [12]. Pearson correlation coefficient provides the measure of linear association between the observed and model predicted values. NSE quantifies the efficiency of a model in predicting the values away from mean, which is theoretically applicable to nonlinear models too [40]. RMSE is the SD of prediction errors and NRMSE is normalized measure of RMSE, which is normalized by the range of actual values. The equations for the calculation of these metrics are presented as follows:

$$r = \frac{\sum_{i=1}^n (y_i - \bar{y})(\hat{y}_i - \bar{\hat{y}})}{\sqrt{\sum_{i=1}^n (y_i - \bar{y})^2} \sqrt{\sum_{i=1}^n (\hat{y}_i - \bar{\hat{y}})^2}} \quad (1)$$

$$\text{NSE} = 1 - \frac{\sum_{i=1}^n (y_i - \hat{y}_i)^2}{\sum_{i=1}^n (y_i - \bar{y})^2} \quad (2)$$

$$\text{RMSE} = \sqrt{\frac{1}{n} \sum_{i=1}^n (\hat{y}_i - y_i)^2} \quad (3)$$

$$\text{NRMSE} = \frac{\text{RMSE}}{y_{\max} - y_{\min}} \times 100 \quad (4)$$

where y_i = observed values; \hat{y}_i = predicted values; n = number of samples; \bar{y} = mean of observed values; y_{\max} = maximum of observed values; y_{\min} = minimum of observed values.

IV. RESULTS

Numerous experiments were carried out to develop the most appropriate model for CACC prediction. The efficacy of outlier tree detection and use of CAE features for CACC modeling are presented and discussed by reporting the results of different experiments in the following sections.

A. Outlier Trees

MDS was performed using the CAE features of each month’s HS image for identification of outlier trees. TIDs 90 and 92 were, respectively, recognized as outlier trees from the HS images of June and July month, which can be identified in Fig. 6(a) and (b), respectively, using a red dotted circle. Similarly, TIDs 2 and 107 were identified as outliers in case of October month’s image [see Fig. 6(c)]. The outlier trees can affect the CACC modeling and reduce the prediction ability of the models. Experiments were carried out with (i.e., considering 83 reference trees) and without (i.e., considering 79 reference trees) outlier trees to evaluate the influence of outlier trees on model performance (see Table II). Both the experiments were performed using 264 HS

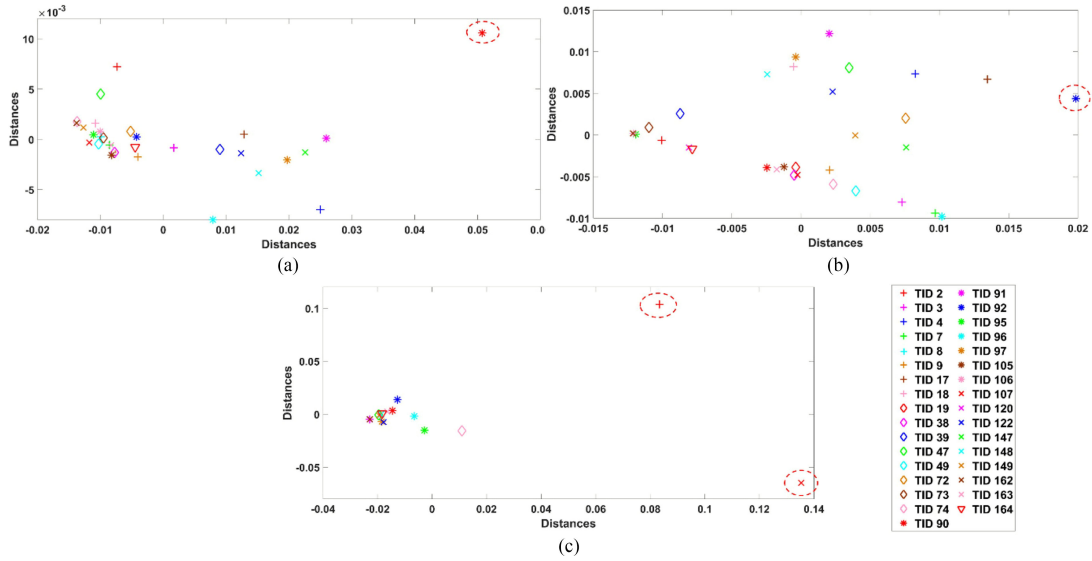


Fig. 6. MDS visualization of CAE features of (a) June (b) July and (c) October month's data [Outlier trees: TID 90 (June), TID 92 (July), TID 2, 107 (October)].

TABLE II
CACC MODELING PERFORMANCES WITH AND WITHOUT OUTLIER TREES

Samples	Training Results				Testing Results			
	r	NSE	RMSE ² ($\mu\text{g}/\text{cm}^2$)	NRMSE (%)	r	NSE	RMSE ² ($\mu\text{g}/\text{cm}^2$)	NRMSE (%)
83	0.84±0.04	0.61±0.06	3.16±0.29	12.1±1.3	0.51±0.12	0.19±0.14	4.20±0.83	16.2±2.9
79	0.84±0.03	0.61±0.05	3.11±0.27	12.0±1.2	0.51±0.08	0.24±0.07	3.98±0.61	15.4±2.1

TABLE III
PERFORMANCES OF CACC MODELING (WITH GPR) CONSIDERING DIFFERENT TRIALS FOR A FIXED NUMBER OF CAE FEATURES

32 CAE features	Trials	Training Results				Testing Results			
		r	NSE	RMSE ($\mu\text{g}/\text{cm}^2$)	NRMSE (%)	r	NSE	RMSE ($\mu\text{g}/\text{cm}^2$)	NRMSE (%)
	1	0.79±0.04	0.57±0.05	3.27±0.29	12.6±1.1	0.58±0.07	0.32±0.09	3.77±0.64	14.5±2.5
	2	0.80±0.04	0.58±0.05	3.20±0.24	12.3±0.9	0.60±0.07	0.34±0.08	3.70±0.59	14.2±2.3
	3	0.77±0.04	0.55±0.06	3.35±0.26	12.9±1.0	0.62±0.10	0.36±0.12	3.66±0.73	14.1±2.8
	4	0.78±0.04	0.56±0.05	3.30±0.27	12.7±1.1	0.61±0.06	0.34±0.09	3.70±0.61	14.2±2.3
	5	0.76±0.02	0.54±0.03	3.39±0.19	13.0±0.7	0.61±0.06	0.35±0.08	3.67±0.60	14.1±2.3
	Mean	0.78±0.03	0.56±0.04	3.30±0.22	12.7±0.8	0.60±0.06	0.34±0.08	3.70±0.54	14.2±2.1

bands in the GPR model. It has been observed that with the removal of outlier trees average NSE, RMSE, and NRMSE of testing datasets are improved. In order to check the statistical significance of the improvement, the means of the squared prediction errors from the two experiments were compared using two samples *t*-test and the means of the errors were statistically different with a significance level of 0.10. The experiments (see Table II) with regression model proved the significance of outlier tree detection in order to achieve better model performance. Hence, all further experiments were carried out with 79 reference samples.

B. Performance of CACC Prediction With CAE Features

The optimal number of CAE features, which can predict CACC efficiently, depends on the used dataset. Number of CAE

features may change for different datasets. Hence, different numbers of CAE features, varying from 8 to 256 (i.e., 8, 16, 32, 64, 128, and 256), were experimented for CACC prediction. For each experiment with a specific number of features, CAE network was trained five times and CACC was modeled ten times with each training resulted features. The results from the CAE network training trials with 32 features are reported in Table III. The average RMSE of the testing data ranged between 3.67 to 3.77 $\mu\text{g}/\text{cm}^2$. The last row of Table III presents the average performance of 50 iterations (i.e., 5×10). The average performances of 50 iterations considering different sets of CAE features are reported in Table IV. It was observed that all sets of CAE features provide almost similar performances. However, 32 CAE features were able to predict the CACC of testing samples more efficiently (i.e., better NSE, RMSE, and NRMSE) compared to other sets of features (see Table IV).

TABLE IV
PERFORMANCES OF CACC MODELING USING DIFFERENT NUMBERS OF CAE FEATURES IN GPR MODEL

Features	Training Results				Testing Results			
	r	NSE	RMSE ² ($\mu\text{g}/\text{cm}^2$)	NRMSE (%)	r	NSE	RMSE ² ($\mu\text{g}/\text{cm}^2$)	NRMSE (%)
8 CAE	0.77±0.05	0.54±0.06	3.35±0.27	12.9±1.0	0.59±0.08	0.32±0.10	3.76±0.51	14.4±1.9
16 CAE	0.77±0.06	0.55±0.07	3.34±0.31	12.8±1.2	0.60±0.07	0.33±0.09	3.73±0.52	14.4±2.0
32 CAE	0.78±0.03	0.56±0.04	3.30±0.22	12.7±0.8	0.60±0.06	0.34±0.08	3.70±0.54	14.2±2.1
64 CAE	0.78±0.05	0.55±0.07	3.31±0.24	12.7±0.9	0.58±0.07	0.31±0.09	3.76±0.49	14.7±1.9
128 CAE	0.80±0.05	0.57±0.06	3.24±0.26	12.4±1.0	0.59±0.06	0.33±0.08	3.73±0.51	14.3±1.9
256 CAE	0.78±0.04	0.56±0.05	3.28±0.20	12.6±0.8	0.60±0.06	0.33±0.08	3.72±0.51	14.3±1.9

TABLE V
COMPARISON OF CACC MODELING PERFORMANCES WITH HS BANDS AND CAE FEATURES

Regression model	Training Results				Testing Results			
	r	NSE	RMSE ² ($\mu\text{g}/\text{cm}^2$)	NRMSE (%)	r	NSE	RMSE ² ($\mu\text{g}/\text{cm}^2$)	NRMSE (%)
264 HS bands								
GPR	0.84±0.03	0.61±0.05	3.11±0.27	12.0±1.2	0.51±0.08	0.24±0.07	3.98±0.61	15.4±2.1
SVR	0.83±0.04	0.64±0.07	2.97±0.32	11.4±1.2	0.52±0.09	0.22±0.11	4.02±0.60	15.5±2.3
32 CAE features								
GPR	0.78±0.03	0.56±0.04	3.30±0.22	12.7±0.8	0.60±0.06	0.34±0.08	3.70±0.54	14.2±2.1
SVR	0.77±0.05	0.56±0.06	3.28±0.30	12.6±1.2	0.59±0.07	0.31±0.09	3.79±0.51	14.6±2.0

TABLE VI
PERFORMANCES OF CACC MODELING BY CHANGING THE TREE CANOPY MASK AREA

Tree canopy area	Training Results				Testing Results			
	r	NSE	RMSE ² ($\mu\text{g}/\text{cm}^2$)	NRMSE (%)	r	NSE	RMSE ² ($\mu\text{g}/\text{cm}^2$)	NRMSE (%)
32 CAE features								
Provided Canopy area	0.78±0.03	0.56±0.04	3.30±0.22	12.7±0.8	0.60±0.06	0.34±0.08	3.70±0.54	14.2±2.1
25×25 patch from Tree centroid	0.82±0.04	0.60±0.06	3.14±0.26	12.0±1.0	0.64±0.08	0.38±0.09	3.67±0.51	14.1±2.0

C. Comparison of CAE Features With HS Bands

In this section, performances of HS bands and best CAE feature-based models were compared (see Table V). CAE features were consistently performing better with the testing samples considering both GPR and SVR based modeling.

Here, we have also compared the performances of GPR and SVR models by considering the HS bands as well as the CAE features as independent variables (see Table V). GPR generally provided better prediction performances (in terms of NSE, RMSE, NRMSE) for testing samples in both the cases. Therefore, all the experiments, investigated in this study, considered the GPR model for modeling and prediction of CACC.

D. Evaluation of the Reliability of Tree Canopy Mask

The tree canopy masks, available in the dataset, were created using the digital surface model and digital terrain model data in the Watershed algorithm [41], [42]. These masks do not provide precise canopy areas of the pear trees. Some masks exclude the portion of tree canopy area, while some other masks include some parts of background pixels. These imperfect canopy masks may influence the model performance. Hence, experiments were performed to check the reliability of the tree canopy masks.

In order to achieve this goal, a patch of size 25×25 was identified from the centroid of each tree and considered as tree canopy area for averaging the feature values. Patch size 25 was chosen because of the fact that almost all the trees have more than 625 pixels within their canopy area. However, patch size of 21, 23, 27, and 29 were also experimented with but 25 was providing better performance compared to others. We have reported the training and testing results only for the patch size of 25 in Table VI. It was observed that with the use of 25×25 patch-based canopy area, training and testing both performances were improved to some extent, when compared with the provided tree canopy mask area.

E. CACC Mapping for all Pear Trees

At the end, CACC of all the Pear trees were estimated for the three months (i.e., June, July, and October) using the 32 CAE features of HS data and presented in Figs. 7–9. Figs. 7–9 also present the reference CACC and zoomed-in view of some specific trees for comparing the reference CACC with the predicted CACC. Though predicted CACC was estimated for all the trees, the zoomed-in view of predicted CACC only presents the predicted values that are shown in the zoomed-in view of

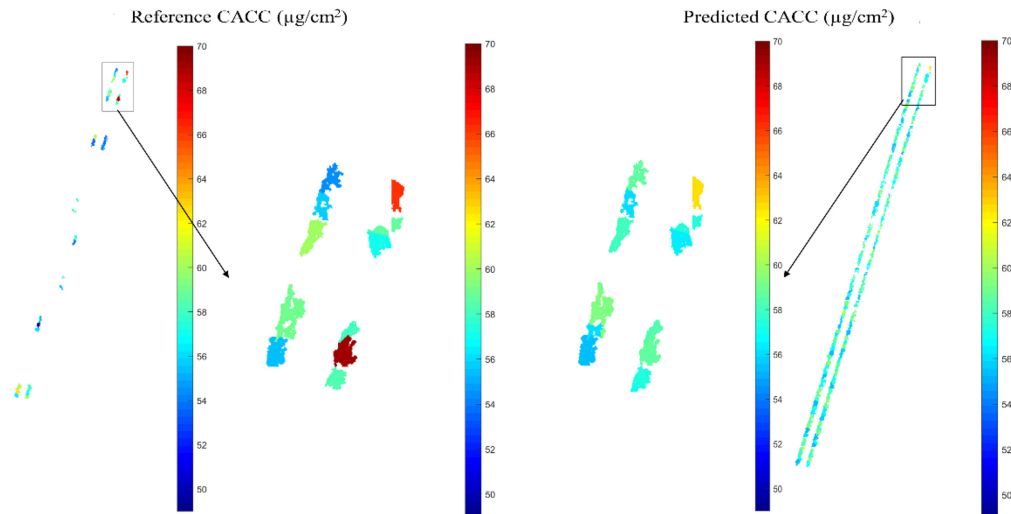


Fig. 7. CACC map of Pear trees for June month.

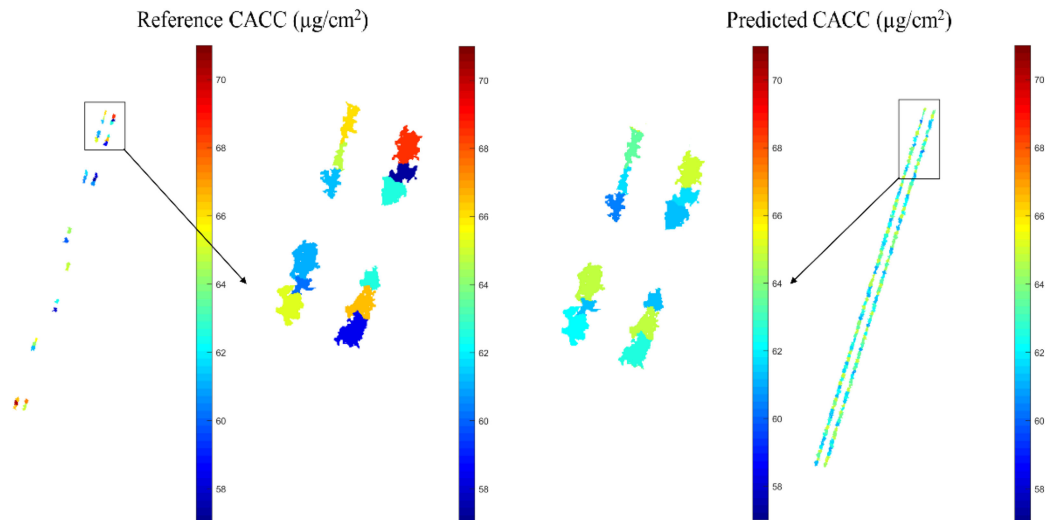


Fig. 8. CACC map of Pear trees for July month.

reference map. It has been observed that the ranges of predicted CACC are narrowed down compared to the reference CACC. For example, in case of June month (see Fig. 7), predicted CACC is ranging between 52 and 64 $\mu\text{g}/\text{cm}^2$, whereas reference CACC range is 50–70 $\mu\text{g}/\text{cm}^2$. However, CACC of most of the trees are predicted closely to the reference values. In case of October month's predicted map (see Fig. 9), most of the trees of right row do not show any estimated value due to unavailability of HS data over those locations.

V. DISCUSSION

This article proposed CAE-based high-level features extraction from HS data for prediction of CACC of pear trees. We have performed MDS on the CAE features in order to detect presence of any anomaly (or outlier) among the trees prior to CACC modeling.

MDS has identified four outlier trees (i.e., one from each June and July, and two from October month's samples) and by removing these trees from the CACC modeling process, the prediction accuracy was improved significantly (at significance level of 0.10). However, we did not have enough ground-truth information to investigate the real reason of inconsistency or anomaly present in the pear trees. Since, we were not involved with the data collection process, we are not able to provide any physiological explanation behind the detection of outlier trees. In this study, detection of outlier trees was completely data driven and depended on the reflectance patterns of the tree canopy area.

CACC prediction was carried out considering different numbers of CAE features (i.e., 8, 16, 32, 64, 128, and 256). CAE features extraction network was run for five iterations and for each iteration CACC was modeled with ten random trials. The consistent performances with several iterations prove the generalization of the CAE architecture to extract the salient

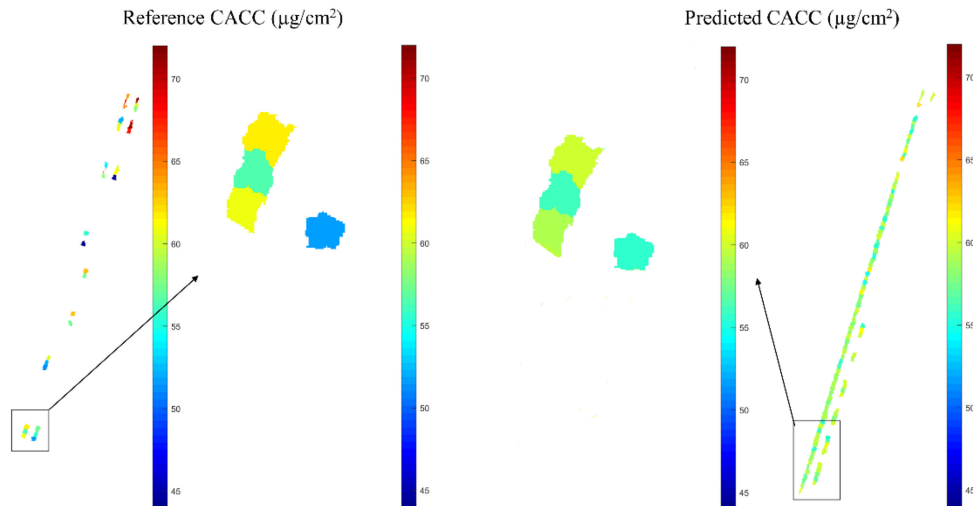


Fig. 9. CACC map of Pear trees for October month.

features and the effectiveness of the CAE features in predicting CACC with any set of training samples. More or less similar performances with the change in numbers of CAE features implies that use of the CAE architecture to extract the features has more significance than the selection of optimal number of features for CACC prediction with this dataset. However, we have selected 32 CAE features as optimal for CACC prediction because of its comparatively better performance with the testing samples and preferable consistency in the performances of training and testing samples. For example, 128 CAE features were providing best performance in case of training samples but not optimal with testing samples, which may raise some chance of overfitting.

CAE features learn the unsupervised deep spectral-spatial representation of the HS data and reduce the redundancy present in the data, which helps in improving the CACC prediction performance, as compared to the use of original HS bands. Since large numbers of contiguous narrow spectral bands introduce redundancy in the data, original HS bands (i.e., without using any feature extraction technique) are not able to perform efficiently. This phenomenon is commonly observable in the classification studies. Hence, our experimental analysis supported the basic characteristics of high-dimensional HS data, where extraction of spectral-spatial features is very significant in order to achieve the optimal performance.

Reliability of the tree canopy masks was evaluated by considering a 25×25 patch from the centre part of the canopy. Though this experiment did not show much significant improvement in performance, this type of analysis is important to check the reliability of the automated watershed algorithm-based tree canopy mask area. Here, the assumed patch size of 25 considers only the center canopy area instead of the whole canopy area, which again may not provide the precise average representation of the features. Manual delineation of tree canopy area can be the best solution but may not be feasible in case of large number of tree samples. Hence, there is a need of better automated algorithm for delineation of tree canopy areas. This emphasizes

the need of more accurate tree canopy area mask in order to get better representation of the whole canopy and achieve better performance.

The figures (see Figs. 7–9) with CACC mapping signify that the tree samples, which have reference CACC close to the minimum or maximum values, were predicted very poorly. In Fig. 7 (i.e., for June month), we can identify three such trees, where two trees have high range values (i.e., $\sim 68\text{--}70 \mu\text{g}/\text{cm}^2$) of reference CACC and another tree (which is TID 90, MDS detected outlier tree) has in the minimum range (i.e., $\sim 52 \mu\text{g}/\text{cm}^2$). Predicted CACC of these trees are ranges between 60 and $62 \mu\text{g}/\text{cm}^2$ approximately. Here, an approximate error of $8 \mu\text{g}/\text{cm}^2$ can be observed for these three trees. Similarly, in case of July (see Fig. 8) and October (see Fig. 9) months' CACC maps, few trees can be identified which have an error of $4 \mu\text{g}/\text{cm}^2$ but this error is not as high as June month's.

VI. CONCLUSION

In this article, we have proposed the use of CAE features, derived from HS data, for CACC modeling of pear trees. The CAE features were proven to be more effective in CACC modeling compared to the HS bands. Different numbers of CAE features were utilized for CACC modeling and 32 CAE features were found to be providing better modeling performance compared to others. Use of the CAE features for CACC modeling reduced average RMSE by 7.03%. We have promoted the use of MDS technique for outlier tree detection prior to CACC modeling, which was improving the performances significantly. Four trees were identified as outliers among the 83 sample trees. With the removal of these outlier trees prior to CACC modeling, average RMSE was reduced by 5.24%. The combination of MDS and CAE for CACC modeling reduced average RMSE by 11.9%. We have investigated the reliability of the tree canopy masks and it was observed that with the consideration of 25×25 patch from the tree centroid as tree canopy, average RMSE was reduced by 0.81%.

This study has a few limitations such as, 1) number of available reference tree samples is too small; 2) unavailability of reference CACC for all the months during the growing period; 3) lack of ground-truth information to enquire the real cause behind anomalies of pear trees; and 4) lack of high precision tree canopy mask area.

Availability of precise tree canopy masks is an important issue, which requires further investigation. The real reason of anomaly present in the pear trees can be explored with the real-time observations and this anomaly or outlier tree detection process can be fully automated as a future work. The proposed methodology can be extended and investigated with more numbers of reference samples in the presence of reliable tree canopy mask for better generalization of the model and better prediction of CACC. This approach can be employed for estimation of biophysical and biochemical variables of different types of vegetation or trees.

ACKNOWLEDGMENT

The authors would like to thank the HYPERTEMP Project group and BELAIR HESBANIA 2017 dataset provider for sharing the data. S. Paul would like to thank National Institute of Advanced Industrial Science and Technology (AIST), Japan for providing the opportunity for Technical Training and financial support to carry out this research work with the Geoinformation Science Research Team (GSRT), Artificial Intelligence Research Center (AIRC), AIST

REFERENCES

- [1] M. Pérez-Patricio *et al.*, "Optical method for estimating the chlorophyll contents in plant leaves," *Sensors*, vol. 18, 2018, Art. no. 650.
- [2] A. Kamilaris, A. Kartakoullis, and F. X. Prenafeta-Boldú, "A review on the practice of big data analysis in agriculture," *Comput. Electron. Agriculture*, vol. 143, pp. 23–37, 2017.
- [3] G. Sylvester, *E-Agriculture in Action: Drones for Agriculture*. Bangkok: Food and Agriculture Organization of the United Nations and International Telecommunication Union, 2018.
- [4] D. Li and C. Zhao, "Computer and Computing Technologies in Agriculture XI," in *Proc. 11th IFIP WG 5.14 Int. Conf.*, August 12–15, 2017, 2019.
- [5] H. Pei, C. Li, H. Feng, G. Yang, M. Liu, and Z. Wu, "Hyperspectral estimation methods for chlorophyll content of apple based on random forest," in *Proc. Int. Conf. Comput. Technol. Agriculture*, 2017, pp. 194–207.
- [6] A. A. Gitelson, A. Vina, V. Ciganda, D. C. Rundquist, and T. J. Arkebauer, "Remote estimation of canopy chlorophyll content in crops," *Geophys. Res. Lett.*, vol. 32, no. 8, pp. L08403.1–L08403.4, 2005.
- [7] M. R. Steele, A. A. Gitelson, and D. C. Rundquist, "A comparison of two techniques for nondestructive measurement of chlorophyll content in grapevine leaves," *Agronomy J.*, vol. 100, pp. 779–782, 2008.
- [8] C. Li *et al.*, "Estimating apple tree canopy chlorophyll content based on Sentinel-2A remote sensing imaging," *Scientific Rep.*, vol. 8, 2018, Art. no. 3756.
- [9] X. Ma, J. Feng, H. Guan, and G. Liu, "Prediction of chlorophyll content in different light areas of apple tree canopies based on the color characteristics of 3D reconstruction," *Remote Sens.*, vol. 10, 2018, Art. no. 429.
- [10] F. Dell'Acqua, P. Gamba, and G. Lisini, "Urban land cover mapping using hyperspectral and multispectral VHR sensors: Spatial versus spectral resolution," in *Proc. URBAN, IAPRS*, Mar. 2005, vol. XXXVI, p. 1416.
- [11] J. Degerickx, D. A. Roberts, J. P. McFadden, M. Hermy, and B. Somers, "Urban tree health assessment using airborne hyperspectral and LiDAR imagery," *Int. J. Appl. Earth Observ. Geoinform.*, vol. 73, pp. 26–38, 2018.
- [12] Y. Vanbrabant, L. Tits, S. Delalieux, K. Pauly, W. Verjans, and B. Somers, "Multitemporal chlorophyll mapping in pome fruit orchards from remotely piloted aircraft systems," *Remote Sens.*, vol. 11, 2019, Art. no. 1468.
- [13] J. A. Berni, P. J. Zarco-Tejada, L. Suárez, and E. Fereres, "Thermal and narrowband multispectral remote sensing for vegetation monitoring from an unmanned aerial vehicle," *IEEE Trans. Geosci. Remote Sens.*, vol. 47, no. 3, pp. 722–738, Mar. 2009.
- [14] J. Verrelst *et al.*, "Optical remote sensing and the retrieval of terrestrial vegetation bio-geophysical properties—a review," *ISPRS J. Photogrammetry Remote Sens.*, vol. 108, pp. 273–290, 2015.
- [15] C. J. Tucker, "Red and photographic infrared linear combinations for monitoring vegetation," *Remote Sens. Environ.*, vol. 8, pp. 127–150, 1979.
- [16] J. Gamon, J. Penuelas, and C. Field, "A narrow-waveband spectral index that tracks diurnal changes in photosynthetic efficiency," *Remote Sens. Environ.*, vol. 41, pp. 35–44, 1992.
- [17] A. Harris, J. Gamon, G. Pastorello, and C. Wong, "Retrieval of the photochemical reflectance index for assessing xanthophyll cycle activity: A comparison of near-surface optical sensors," *Biogeosciences*, vol. 11, pp. 6277–6292, 2014.
- [18] G. Rondeaux, M. Steven, and F. Baret, "Optimization of soil-adjusted vegetation indices," *Remote Sens. Environ.*, vol. 55, pp. 95–107, 1996.
- [19] C. Daughtry, C. Walthall, M. Kim, E. B. De Colstoun, and J. McMurtry III, "Estimating corn leaf chlorophyll concentration from leaf and canopy reflectance," *Remote Sens. Environ.*, vol. 74, pp. 229–239, 2000.
- [20] D. Haboudane, J. R. Miller, N. Tremblay, P. J. Zarco-Tejada, and L. Dextraze, "Integrated narrow-band vegetation indices for prediction of crop chlorophyll content for application to precision agriculture," *Remote Sens. Environ.*, vol. 81, pp. 416–426, 2002.
- [21] S. Gandia, G. Fernández, J. García, and J. Moreno, "Retrieval of vegetation biophysical variables from CHRIS/PROBA data in the SPARC campaign," *Esa Sp.*, vol. 578, pp. 40–48, 2004.
- [22] E. R. Hunt Jr, P. C. Doraiswamy, J. E. McMurtry, C. S. Daughtry, E. M. Perry, and B. Akhmedov, "A visible band index for remote sensing leaf chlorophyll content at the canopy scale," *Int. J. Appl. Earth Observ. Geoinform.*, vol. 21, pp. 103–112, 2013.
- [23] J. Verrelst, L. Alonso, G. Camps-Valls, J. Delegido, and J. Moreno, "Retrieval of vegetation biophysical parameters using Gaussian process techniques," *IEEE Trans. Geosci. Remote Sens.*, vol. 50, no. 5, pp. 1832–1843, May 2011.
- [24] G. Camps-Valls, L. Bruzzone, J. L. Rojo-Alvarez, and F. Melgani, "Robust support vector regression for biophysical variable estimation from remotely sensed images," *IEEE Geosci. Remote Sens. Lett.*, vol. 3, no. 3, pp. 339–343, Jul. 2006.
- [25] Y. Bazi and F. Melgani, "Semisupervised PSO-SVM regression for biophysical parameter estimation," *IEEE Trans. Geosci. Remote Sens.*, vol. 45, no. 6, pp. 1887–1895, Jun. 2007.
- [26] G. Camps-Valls, L. Gómez-Chova, J. Muñoz-Marí, J. Vila-Francis, J. Amorós-López, and J. Calpe-Maravilla, "Retrieval of oceanic chlorophyll concentration with relevance vector machines," *Remote Sens. Environ.*, vol. 105, pp. 23–33, 2006.
- [27] J. Geng, J. Fan, H. Wang, X. Ma, B. Li, and F. Chen, "High-resolution SAR image classification via deep convolutional autoencoders," *IEEE Geosci. Remote Sens. Lett.*, vol. 12, no. 11, pp. 2351–2355, Nov. 2015.
- [28] J. Zabalza *et al.*, "Novel segmented stacked autoencoder for effective dimensionality reduction and feature extraction in hyperspectral imaging," *Neurocomputing*, vol. 185, pp. 1–10, 2016.
- [29] X. Ma, H. Wang, and J. Geng, "Spectral-spatial classification of hyperspectral image based on deep auto-encoder," *IEEE J. Sel. Topics Appl. Earth Observ. Remote Sens.*, vol. 9, no. 9, pp. 4073–4085, 2016.
- [30] S. Paul and D. N. Kumar, "Spectral-spatial classification of hyperspectral data with mutual information based segmented stacked autoencoder approach," *ISPRS J. Photogrammetry Remote Sens.*, vol. 138, pp. 265–280, 2018.
- [31] Y. Chen, Z. Lin, X. Zhao, G. Wang, and Y. Gu, "Deep learning-based classification of hyperspectral data," *IEEE J. Sel. Topics Appl. Earth Observ. Remote Sens.*, vol. 7, no. 6, pp. 2094–2107, Jun. 2014.
- [32] B. Leng, S. Guo, X. Zhang, and Z. Xiong, "3D object retrieval with stacked local convolutional autoencoder," *Signal Process.*, vol. 112, pp. 119–128, 2015.
- [33] W. Cui, Q. Zhou, and Z. Zheng, "Application of a hybrid model based on a convolutional auto-encoder and convolutional neural network in object-oriented remote sensing classification," *Algorithms*, vol. 11, 2018, Art. no. 9.

- [34] L. Blouvshtein and D. Cohen-Or, "Outlier detection for robust multi-dimensional scaling," *IEEE Trans. Pattern Anal. Mach. Intell.*, vol. 41, no. 9, pp. 2273–2279, Sep. 2018.
- [35] X. Guo, X. Liu, E. Zhu, and J. Yin, "Deep clustering with convolutional autoencoders," in *Proc. Int. Conf. Neural Inf. Process.*, 2017, pp. 373–382.
- [36] Y. Zhang, "A better autoencoder for image: Convolutional autoencoder," in *ICONIP17-DCEC*, 2018. [Online]. Available: http://users.cecs.anu.edu.au/Tom.Gedeon/conf/ABCs2018/paper/ABCs2018_paper_58.pdf. Accessed on Mar. 23 2017
- [37] M. D. Zeiler, "ADADELTA: An adaptive learning rate method," 2012. [Online]. Available: <https://arxiv.org/abs/1212.5701>
- [38] J. B. Kruskal, "Nonmetric multidimensional scaling: A numerical method," *Psychometrika*, vol. 29, pp. 115–129, 1964.
- [39] C. Chollet, "Keras: The python deep learning library," 2015. [Online]. Available: <https://keras.io>
- [40] L. Karthikeyan, D. N. Kumar, D. Graillot, and S. Gaur, "Prediction of ground water levels in the uplands of a tropical coastal riparian wetland using artificial neural networks," *Water Resour. Manage.*, vol. 27, pp. 871–883, 2013.
- [41] K. Zhao and S. Popescu, "Hierarchical watershed segmentation of canopy height model for multi-scale forest inventory," in *Proc. ISPRS Workshop Laser Scann. SilviLaser*, 2007, pp. 436–441.
- [42] Q. Chen, D. Baldocchi, P. Gong, and M. Kelly, "Isolating individual trees in a savanna woodland using small footprint lidar data," *Photogrammetric Eng. Remote Sens.*, vol. 72, pp. 923–932, 2006.



Subir Paul received the B.Tech. degree in agriculture engineering from Uttar Banga Krishi Viswavidyalaya, West Bengal, India, in 2013 and the M.E. degree in water resources and environmental engineering from the Department of Civil Engineering, Indian Institute of Science (IISc), Bengaluru, India, in 2015. He is currently working toward the Ph.D. degree with the Department of Civil Engineering, IISc, Bengaluru, India.

His current research interests include applications of multispectral and hyperspectral remote sensing images for land cover and crop classification and estimation of biophysical and biochemical variables using advanced machine learning or deep learning techniques. For more information, please visit: <https://sites.google.com/site/subirpaul241191/>



Vinayaraj Poliyapram received the Ph.D. degree from Osaka City University, Osaka, Japan in 2017 and the master's degree from Mangalore University, Karnataka, India, in 2009.

He pursued his Ph.D. with a Japanese Government Scholarship (MEXT). He is currently a Postdoctoral Researcher with the National Institute of Advanced Industrial Science and Technology (AIST), Japan. From 2009 to 2011, he was a Research Fellow with the National Institute of Technology (NIO), India. His current research interests are satellite image processing

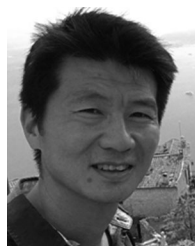
and deep learning application for segmentation of multispectral, hyperspectral, SAR images, and LIDAR point cloud.



Nevrez Imamoğlu received the Ph.D. degree from Chiba University, Chiba, Japan in 2015. He pursued his Ph.D. with a Japanese Government Scholarship (MEXT).

He has been a Senior Researcher with Artificial Intelligence Research Center (AIRC), National Institute of Advanced Industrial Science and Technology (AIST), Tokyo, Japan, since April 2016. Before AIST, he was with RIKEN Brain Science Institute as a Researcher and JSPS Foreign Postdoctoral Fellow. He was also with School of Computer

Eng., NTU, Singapore as a Research Associate. His research interests include computer vision, artificial intelligence, remote sensing, intelligent systems, recently with special interests on deep learning for multimodal or multitemporal signal/image analysis, visual attention (saliency detection), classification/object detection/segmentation on satellite images (optical, multispectral, hyperspectral).



Kuniaki Uto received the Ph.D. (Doctor of Engineering) degree from Tokyo Institute of Technology, Tokyo, Japan, in 1999.

He is currently an Assistant Professor with the School of Computing in Tokyo Institute of Technology, Tokyo, Japan. His current field of interests are precision agriculture and phenotyping based on airborne images, optical sensors, and hyperspectral remote sensing. He was a collaborator of the HYPER-TEMP (Multitemporal monitoring of fruit orchard vitality with multisensory BELAIR data) project

funded by the BELSPO (Belgian Science Policy Office).



Ryosuke Nakamura received the Ph.D. degree from Kobe University, Kobe, Japan, in 1996.

He worked with Japan Aerospace Exploration Agency (JAXA) to develop space-borne sensors and the ground-based data analysis system. He is currently with AIRC, AIST as the Team Leader of the Geoinformation Science Research Team. His current field of interests are satellite remote sensing, virtual 3-D/4-D models and their applications for smart city or smart farms. His team works on and develops intelligent and effective analysis engines to handle

rapidly growing geoinformation, such as satellite imagery and aerial photo, to meet scientific and social demand.



D. Nagesh Kumar received the Ph.D. degree from the Department of Civil Engineering, Indian Institute of Science (IISc), Bangalore, India, in 1992.

He was a Boyscast Fellow with the Utah Water Research Laboratory, Utah State University, Logan, UT, USA, in 1999. He has been a Professor with the Department of Civil Engineering, IISc, since May 2002. Earlier, he was with the IIT, Kharagpur, India, and National Remote Sensing Centre, Hyderabad, India. He is the co-author of six text books and authored more than 200 papers including 118 in peer reviewed

journals. His research interests include climate hydrology, climate change, water resource systems, ANN, evolutionary algorithms, fuzzy logic, MCDM, and remote sensing and GIS applications in water resource engineering. For more information, please visit: <http://civil.iisc.ac.in/~nagesh/>